Journal of Power Sources 454 (2020) 227907

Contents lists available at ScienceDirect

Journal of Power Sources

journal homepage: www.elsevier.com/locate/jpowsour

Improved adhesion of cross-linked binder and SiO_2-coating enhances structural and cyclic stability of silicon electrodes for lithium-ion batteries

Sen Sun [a,1], Donglin He [a,1], Ping Li [a,*], Ying Liu [a], Qi Wan [b], Qiwei Tan [a], Zhiwei Liu [a], Fuqiang An [a], Gaoxiang Gong [a], Xuanhui Qu [a,c,d,**]

[a] Beijing Advanced Innovation Center for Materials Genome Engineering, Institute for Advanced Materials and Technology, University of Science and Technology Beijing, Beijing, 100083, China
[b] School of Materials Science and Engineering, Southwest University of Science and Technology, Mianyang, 621010, China
[c] Beijing Laboratory of Metallic Materials and Processing for Modern Transportation, University of Science and Technology Beijing, Beijing, 100083, China
[d] The State Key Laboratory for Advanced Metals and Materials, University of Science and Technology Beijing, Beijing, 100083, China

HIGHLIGHTS

- The cross-linked PAA and DS binder is prepared by in situ synthesis method.
- A strong electrode is constructed.
- The Si@SiO_2-PAA-GL electrode exhibits remarkable performance.

ARTICLE INFO

Keywords:
SiO_2 coating
Cross-linked PAA-Glycerol binder
Silicon anode
Li-ion battery

ABSTRACT

Silicon (Si) has been considered as a promising alternative anode material for high energy density lithium-ion batteries because of high theoretical capacity, low cost, environmentally benign, and abundant source. But the huge volume change during cycles greatly hinders the application of Si anodes. Constructing robust electrode structures via effective binders are still a challenge. Herein, a cross-linked polyacrylic acid and glycerol (PAA-GL) binder is synthesized in situ and a surface coating of silicon dioxide is obtained on silicon nanoparticles (Si@SiO_2), both of which together construct a strong electrode. The Cross-linked binder with massive hydroxyl and carboxyl groups possesses luxuriant contact sites to Si@SiO_2, meanwhile, the free carboxyl groups of binder and hydroxyl of Si@SiO_2 offer an enhanced interaction, leading to robust electrode with strong mechanical properties. Except for binder, the SiO_2-modified coat acts as a protective layer to buffer volume change of Si. Therefore, the remarkable structural stability is obtained. In addition, the Si@SiO_2-PAA-GL electrode exhibits excellent electrochemical performance, a high capacity of 1192.7 mA h g^{-1} at 2 C after 500 cycles with a teeny capacity decay rate of 0.0337% per cycle.

1. Introduction

Lithium-ion batteries (LIBs) have become the most widely used secondary battery due to the high energy density, durable cycle lifetime, and environment amity [1–4]. To extend the application of LIBs to fast-developing industrial fields, such as electric vehicles, power grid, and broad-scale energy storage system, LIBs must further break through the limits of the energy density to meet new industry requirements [5–8]. Silicon (Si) is considered to one of the most potential candidate to substitute carbon-based materials due to ultrahigh theoretical capacity of about 4200 mA h g^{-1}, low electrochemical window, and abundant resource [9–12]. However, Si anodes suffer huge volume expansion (>300%) during charge/discharge process, resulting in serious samsh, loss of electrical contact, rapid electrode deterioration, and fast capacity loss. Furthermore, the fragile solid electrolyte interphase (SEI) caused by large volume expansion and retraction of Si particles will continually

* Corresponding author.
** Corresponding author. Beijing Advanced Innovation Center for Materials Genome Engineering, Institute for Advanced Materials and Technology, University of Science and Technology Beijing, Beijing, 100083, China.
E-mail addresses: ustbliping@126.com (P. Li), quxh@ustb.edu.cn (X. Qu).
[1] Authors of Sen Sun and Donglin He contributed equally to this work.

https://doi.org/10.1016/j.jpowsour.2020.227907
Received 1 June 2019; Received in revised form 10 February 2020; Accepted 14 February 2020
Available online 22 February 2020

break and rebuild, so that the lithium ions provided by the positive electrode are consumed massively and rapidly [13,14]. To tackle these issues, novel Si anodes with sundry rationally-designed nanostructures have been developed to relieve the internal stress, such as Si nanowire, Si nanotube, and porous Si nanosphere [3,15–19]. Additionally, the huge volume expansion of Si anodes can also be accommodated through the delicate introduction of void space in nanostructures of yolk-shell, hollow, and porous networks [20–24]. Although the elaborately designed structures are conducive to accommodate the stress derived from Si and keep the integrity of electrode, the complicated synthesis process as well as expensive cost still greatly hinder their actual applications.

Apart from the structural engineering of Si anodes, binders, as an important component in the electrodes, also play vital role in improving the electrochemical performance [25–27]. Significantly, the binders conglutinate the active materials and conductive additives together on copper foil, thus greatly determining the stability of the electrodes [28,29]. However, the commonly used binder of polyvinylidene difluoride (PVDF) cannot satisfy the demand for high energy density Si anodes because of the weak van der Waals interplay among the active materials, conductive additives, and copper foil [30–32]. For the ideal binder for Si anodes, there are some rigorous requirements, such as sufficient mechanical strength, effective connectivity, and excellent chemical stability to overcome the huge volumetric expansion [33]. Recently, some polymer binders have been studied for high-performance Si anodes, including carboxymethyl cellulose (CMC), polyacrylic acid (PAA), polyvinyl alcohol (PVA), guar gum (GG), polyethylene glycol (PEG), chitosan, etc [31,34–36]. As illustrated in Fig. 1a–b, the unmodified polymer binders of CMC and PAA bind Si particles and conductive additives together, but it cannot buffer the frequent expansion and deflation of Si nanoparticles, leading to the disintegration of the electrode. However, the cross-linked binders with superior mechanical ability and 3D network structure can significantly adapt the drastic volume change of Si particles. For instance, Koo et al. developed a cross-linked PAA-CMC binder, which had achieved stable cyclic performance and enhanced coulomb efficiency (88.2%) for Si anode [37]. Song et al. synthesized a robust binder by conjugating CMC with PVA to enhance the cycling stability of Si electrode, and the capacity of PAA-PVA electrode remains 2283 mA h g^{-1} after 100 cycles [38]. Wu et al. synthesized an in situ polymerized conductive polymer binder PANI, which forms a well-connected 3D conductive network structure. The electrode was continuously tested up to 5000 cycles without apparent capacity decay [39]. These aforementioned binders can enhance the electrochemical properties of electrodes to some extent, however, it is still difficult for industrialization at present because of the complex synthetic method and expensive cost. Therefore, it is still necessary to hunt for new binder with simple synthesis, cheap ingredients, and excellent performance for high performance Si anode.

In this work, we developed a modified polyacrylic acid polymer binder with glycerol (PAA-GL) through in-situ dehydration condensation reaction during the preparement of electrode. In addition, the interfacial adhesion between the cross-linked PAA-GL binder and the active material is greatly enhanced by surface functionalization of Si nanoparticles with a silicon oxide coating (Si@SiO_2), improving structure stability of Si@SiO_2 electrode. As schematically shown in Fig. 1c, a cross-linked 3D network binder is produced after modification of the PAA binder, which can significantly maintain the integration of Si@SiO_2 based electrode during repeated cycles because of the enhanced adhesion between PAA-GL binder and SiO_2 coating on the surface of Si. The cross-linked PAA-GL binder has several advantages. First of all, the PAA-GL binder with cross-linked structure displays excellent mechanical stability to release the stress from the volumetric charge of Si nanoparticles. Second, the abundant functional groups on the PAA-GL binder can potentially bind with the OH groups on the SiO_2 layer via chemical interaction, increasing the adhesion ability of PAA-GL binder. Third, the electrode with PAA-GL can be easily prepared by homogeneously mixing Si particles with the glycerol and PAA in the water to produce the slurry without needing toxic and volatile solvents. In addition to the above advantages of binder, the outer SiO_2 coating of Si nanoparticle serves as a buffer layer, promoting the structural stability of electrode and protecting the inner Si from pulverizing. As a result, the Si@SiO_2-PAA-GL electrode exhibits high capacity, high initial coulombic efficiency (88.87%), good rate performance, and remarkable cycling performance (83.13% retention after 500 cycles).

2. Experimental section

2.1. Preparation of Si@SiO_2

Pure Si nanoparticles were purchased from Sigma-Akdrich. Si@SiO_2 particles were prepared by partial oxidation of Si. Typically, 1 g Si nanoparticles was heated at 500 °C for 1h in the air atmosphere, then the Si@SiO_2 particles were obtained.

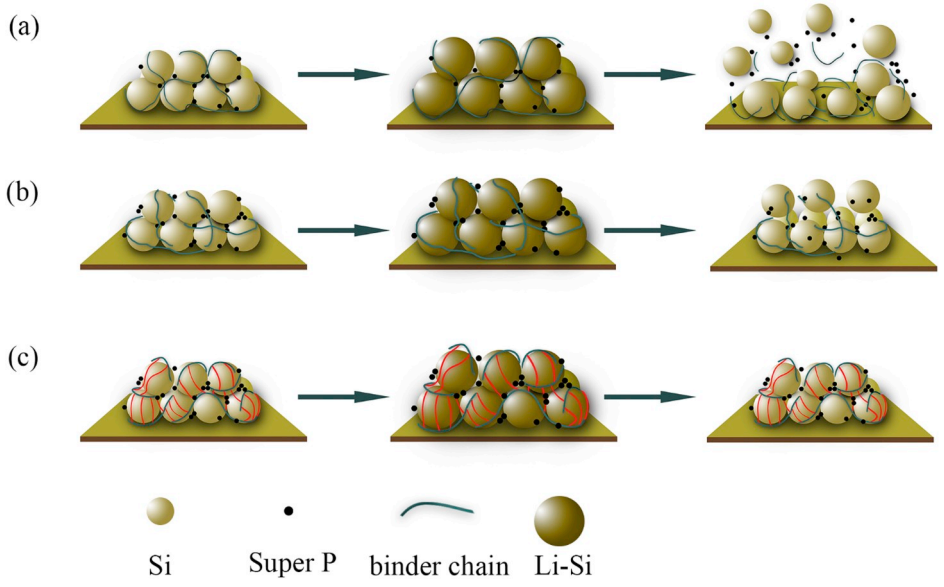

Fig. 1. Schematic illustration of lithiation/delithiation process of Si-based electrode with CMC, PAA, and PAA-GL binders.

2.2. Materials characterization

Scanning electron microscope (SEM, Hitachi SU8020) and transmission electron microscope (TEM, JEM 2100F) were used to characterize the morphology of active materials. The crystal structures of the products were characterized by X-ray diffraction (XRD, Cu Kα radiation). Raman spectroscopy was carried out using 532 nm laser excitation (LabRAM HR Evolution). Fourier transform infrared (FTIR, Thermo Nicolet Corporation Nicolet IS10) spectroscopy and hydrogen nuclear resonance (^{1}H NMR, Bruker 400 MHz) spectroscopy were used to analyze the synthesized polymer binder PAA-GL and the electrode of Si@SiO_2/PAA-GL. The surface chemical states of elements were tested by X-ray photoelectron spectroscopy (XPS, Kratos AXIS spectrometer with a monochromic Al Kα ($h\nu = 1486.69$ eV) radiation).

2.3. Electrochemical measurements

The active materials (Si@SiO_2), binder (CMC, PAA, and PAA-GL), and conductive additives (Super P) were mixed to form homogeneous slurries with a mass ratio of 8:1:1. Then the slurries were coated on a Cu foil and vacuum-dried at 150 °C for 2 h. During vacuum-drying, the thermal condensation reaction occurred to form the cross-linked PAA-GL binder. The Si@SiO_2 mass loading was around 0.5 mg cm^{-2}. In electrochemical characterizations, 2032 type coin cell were fabricated in an Ar atmosphere glove box with Celgard 2400 film as a separator, lithium metal as the counter electrode, and 1 M $LiPF_6$ in a mixture of diethyl carbonate and ethylene carbonate (1:1) with 5 wt% fluoroethylene chloride additive as the electrolyte. The galvanostatic charge and discharge measurement was conducted on a Neware testing system within the voltage window of 0.01 and 2 V vs Li/Li$^+$. Cyclic voltammetry (CV) measurement was tested between 0.01 and 3 V at 0.1 mV s^{-1} on CHI760E electrochemical workstation. Electrochemical impedance spectroscopy (EIS) were performed on a CHI 760E electrochemical workstation in the frequency range from 100 kHz to 0.01 Hz.

2.4. Mechanical properties examinations

The electrode samples were cropped to strips of 20 × 60 mm. For 180° peeling tests, electrode samples prepared with different binders were attached to the 3 M Tape, whereas the backside (aluminum) of the electrode was pasted on a double sided adhesive tape. The peeling force was carried out with 180° peeling tests by pulling the tape at a speed of 60 mm min^{-1} with the universal tension machine Instron 3365. In nano-indention tests, the films of CMC, PAA, and PAA-GL binders were carried on in the Nano Indenter II MTS, and a constant load of 1 mN was applied during the test. Scratch tests were performed in the Universal Micro-Triboteste equipped with a Berkovich diamond indenter with a 100 μm tip.

3. Results and discussion

From Fig. 1, the three kinds of binders were compared, indicating that the cross-linked PAA-GL binder is the most suitable for the electrodes. The cross-linked PAA-GL binder has several advantages. The cross-linked PAA-GL binder was obtained through in-situ dehydration condensation reaction during the preparation of electrode. The reaction mechanism of the *in site* cross-linked binder between PAA and GL is shown in Fig. 2a. The condensation reaction between the –COOH on PAA and –OH on GL occurs at 150 °C under vacuum, achieving the ester groups and generating a cross-linked network structure. The network structure of PAA-GL binder can offer more contact sites, which is conductive to improve mechanical and electrochemical properties of the Si@SiO_2 electrode. However, the cross-liking reaction within Si@SiO_2 electrode is difficult to be tested because of many ingredients in the electrode. Therefore, the pure cross-linked powders were used for further Fourier transform infrared (FTIR) test to investigate the mechanism of the cross-linking between Si@SiO_2 particles and the binder. As shown in Fig. 2b, the characteristic peak of the C═O bonds from the carboxyl on PAA appears at 1710 cm^{-1}, but it moves to higher wavenumber of 1730 cm^{-1} in the spectrum of PAA-GL after modified with the glycerol, proving the formation of ester groups (COO) due to condensation reaction between PAA and GL [37]. There are lots of Si–OH bonds

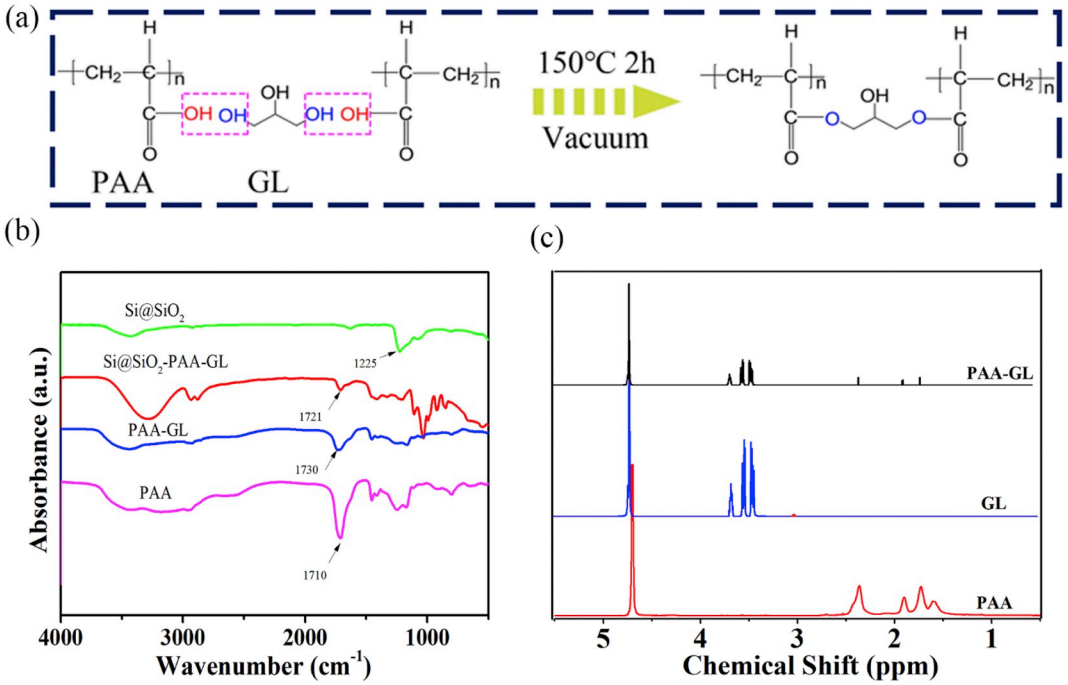

Fig. 2. (a) Schematic illustration of the synthetic process for the cross-linked PAA-GL binder. (b) FTIR spectra of Si@SiO_2, Si@SiO_2-PAA-GL, PAA-GL, and PAA. (c) 1H NMR spectra of PAA, glycerol, and PAA-GL binder.

on the surface of the Si particles, which could be confirmed by the peak around 3400 cm^{-1} in FTIR spectrum of Si@SiO_2 particles [38]. It is reported that the distribution of electron density of –OH groups can change by interaction, reducing the stretching vibration frequencies [40]. Compared with Si-PAA-GL (Fig. S1), the peaks of C═O and Si–OH bonds evidently remove to 1721 and 1077 cm^{-1} in the spectrum of Si@SiO_2-PAA-GL, respectively, indicating that a strong interaction has happened between the Si@SiO_2 particles and PAA-GL binder. This result may be attributed to abundant Si–OH groups on the surface of Si after oxidation [41]. Consequently, the covalent bond between the free COOH of PAA-GL and OH on the surface of Si@SiO_2 forms through the condensation reaction, which can effectually inhibit the large slide of Si particles.

Fig. 2c displays the results of ^1H NMR spectra of GL, PAA, and PAA-GL. The peak at 4.77 ppm is due to the track of unmarked H_2O in D_2O. The proton signals at 2.23–2.50 and 1.5–2.0 ppm are ascribed to the protons in the carbonyl groups and methylene groups of PAA, respectively. The proton signals of the methylene group are found between 3.2 and 3.7 ppm in the glycerol spectra. Comparing to the spectra of GL and PAA, the peaks of PAA-GL spectrum represents the protons resonance in the carbonyl groups and methylene groups. The above results certificate that cross-linked structure of PAA-GL binder has been obtained.

The structure of active materials is crucial for electrochemical performances. To study the structure and composition, the Si@SiO_2 nanoparticles were scientifically characterized. XRD was carried out to investigate the crystallization of prepared samples. From Fig. 3a, the main diffraction peaks of Si@SiO_2 are located at 28.4°, 47.3°, 56.1°, 69.1°, 76.4°, and 88.0°, corresponding to the (111), (220), (311), (400), (331), and (422) plane of crystalline Si (JCPDS No. 27–1402), respectively. In addition to the typical peaks of Si phase, there is no other obvious peaks in the spectrum of Si@SiO_2 particles, confirming the amorphous feature of the outer oxide layer (SiO_2). The crystallinity and purity of Si@SiO_2 were also studied by Raman spectrum. As shown in Fig. 3b, the peak at 500 cm^{-1} corresponds to the representative peak of Si particles, lower than that of bulk Si at 520 cm^{-1}, indicating the nanoscale size of Si particles [42]. The broad peak at 285 cm^{-1} is associated with amorphous silicon oxide layer [43].

The morphology of Si particles before and after heat treatment was recorded with SEM and TEM. From the images of Fig. 3c–d, the average diameters of the Si@SiO_2 particles are 50–100 nm. As plotted in Fig. 3e, the high-resolution TEM (HRTEM) image of pure Si nanoparticle present clear lattice fringes, indicating crystalline state of pure Si. However, an amorphous coating with a thickness of about 5 nm appears on the outer surface of Si particles after heat treatment (Fig. 3f). Furthermore, the scanning TEM (STEM) image and elemental mapping results (Fig. 3g) clearly show the Si@SiO_2 structure with the corresponding Si and O

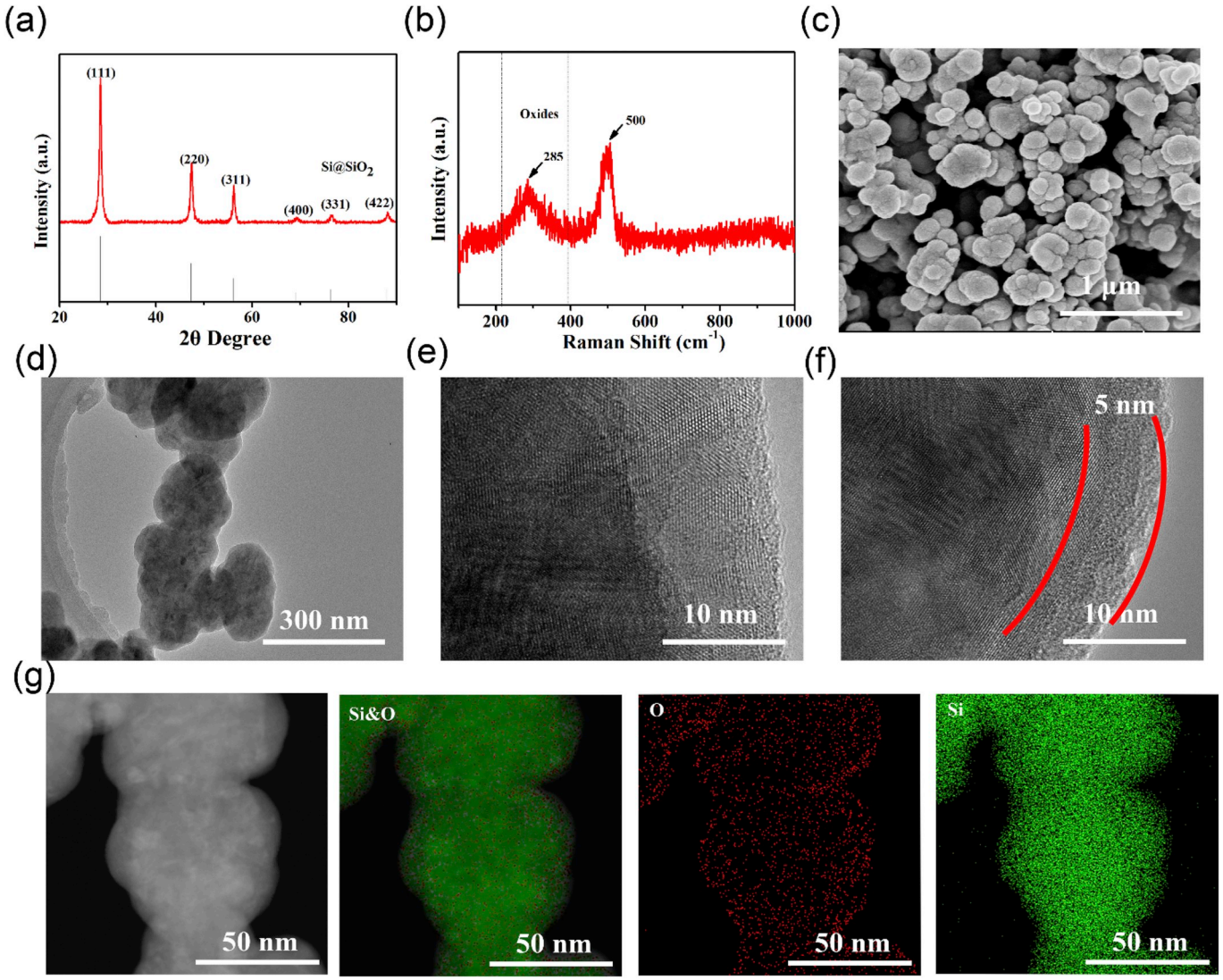

Fig. 3. (a) XRD pattern, (b) Roman pattern, (c) SEM image, and (d) TEM image of Si@SiO_2 particles. HRTEM image of (e) pure Si particles and (f) Si@SiO_2 particles. (g) HAADF-STEM image of the Si@SiO_2 and corresponding elemental mappings.

element. The outline of oxygen element is homogeneously located in the outer surface of Si particles. Besides, the FTIR spectrum of the Si@SiO_2 appears a sharp peak at 1225 cm^{-1}, belonging to the characteristic peak of Si–O–Si, compared with spectrum of pure Si particles without heat treatment (Fig. S2), demonstrating that SiO_2 layer has been successfully formed after the modification process.

In addition to material structure, binder is an important part of electrodes and acts an important role in enhancing cycle lifespan and avoiding irreversible capacity loss. Binder with high mechanical strength could validly buffer drastic volume change of Si particles and ensure structure stability of electrode. Therefore, it is extremely important to examine the mechanical performance of the polymer binder. Firstly, the mechanical performance of binders were assessed by nano-indentation tests (Fig. 4a–c). As shown in Fig. 4a, the indentation force of the PAA-GL binder is higher than that of PAA and CMC binder at the same indentation depth, suggesting that PAA-GL binder is more robust than CMC and PAA binders. Fig. 4b and c displays the modulus and hardness variation with different depth for CMC, PAA, and PAA-GL binders. Generally speaking, a high modulus value suggests powerful binding strength, and a high hardness value represents energy absorb ability and favorable ductile property, which is different from the general brittle glass or crystal material [31]. Therefore, the higher modulus and hardness of the PAA-GL demonstrate that PAA-GL-Si@SiO_2 electrode possesses stronger mechanical performances to resists the stress derived from volume expansion of Si@SiO_2 particles, comparing to CMC and PAA based electrodes.

The peeling measurements were used to quantify the adhesive ability of the binders. As illustrated in Fig. 4d and Fig. S3, the Si@SiO_2-PAA-GL electrode exhibits higher average peeling force (6.44 N) than that of Si@SiO_2-PAA (1.69 N) and Si@SiO_2-CMC electrode (1.30 N), indicating stronger adhesive ability of PAA-GL binder. From the digital images of the electrodes after peeling tests (Fig. 4e), the tape has hardly any active materials tightly attached on Cu foil after peeling off from the Si@SiO_2-PAA-GL electrode, demonstrating strong adhesive force of PAA-GL binder. On the contrary, for Si@SiO_2-CMC and Si@SiO_2-PAA electrodes, a mass of active materials are stripped from Cu foil due to the weaker adhesion of CMC and PAA binders. Strong adhesion of PAA-GL binder can significantly enhance the stability of electrode and improve electrochemical property during charge/discharge cycles.

Friction coefficient of the electrodes were evaluated by scratch tests. The scratch tests can be used to analyze the endurance of binder to the stress derived from the volume change of Si nanoparticles [31,44,45]. Fig. 4f shows that the friction coefficient of the Si@SiO_2-PAA-GL is larger than that of Si@SiO_2-PAA and Si@SiO_2-CMC, certifying a higher adhesive strength and better mechanical property of PAA-GL based electrode. Fig. 4g–i illustrate the morphologies of the Si@SiO_2 electrodes with diverse binders after the scratch tests. The scratched surface of Si@SiO_2-PAA-GL electrode is very smooth without cracks (Fig. 4i).

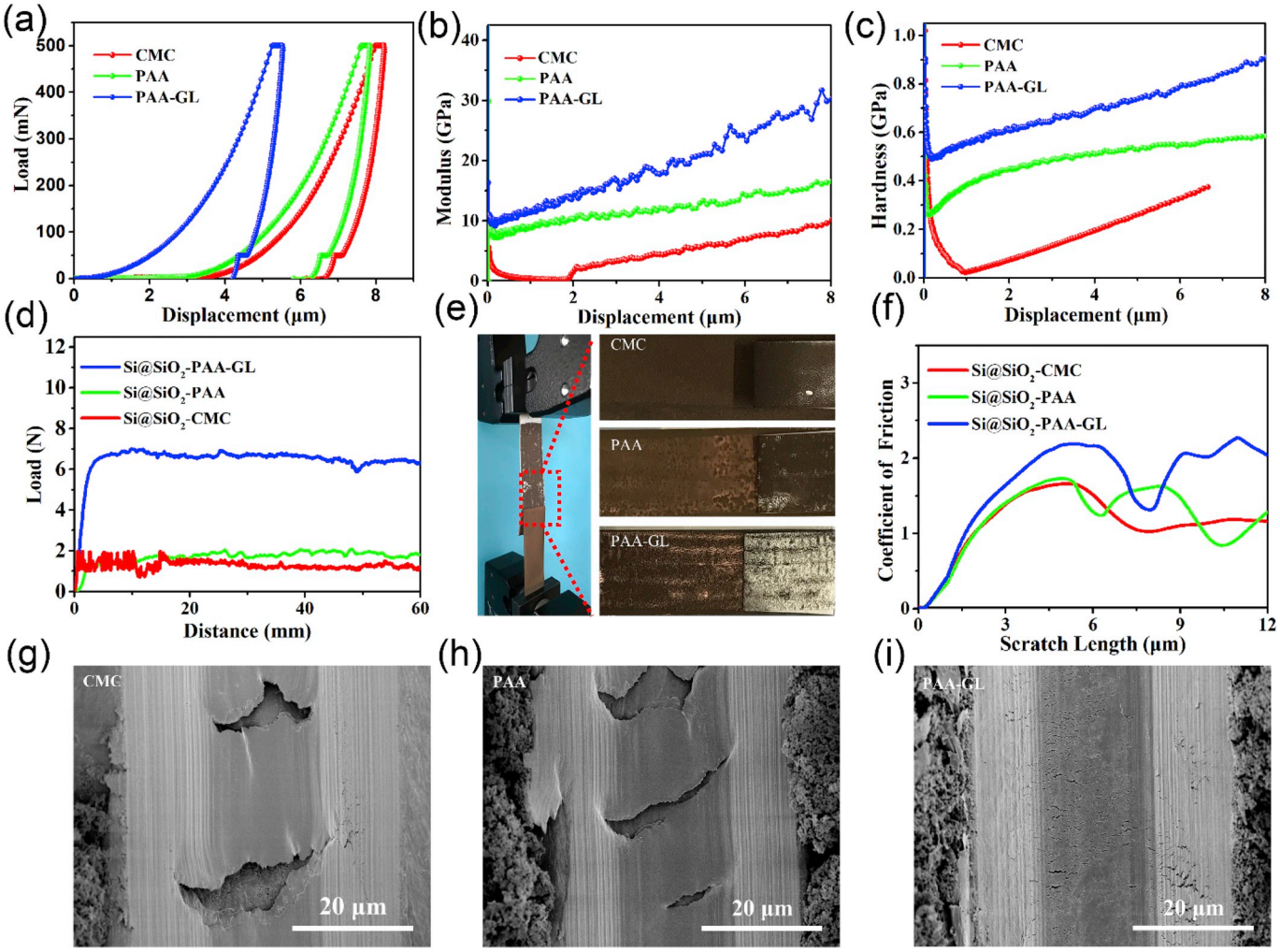

Fig. 4. (a) The load-indentation depth curve, (b) elastic modulus, and (c) hardness of the CMC, PAA, and PAA-GL binder films. (d) Peeling force-displacement curves of the Si@SiO_2 electrodes. (e) Detailed optical image of the peeling test setup and electrodes after peeling tests. (f) The friction coefficient of Si@SiO_2 electrodes. (g–i) SEM images of Si@SiO_2-CMC (g), Si@SiO_2-PAA (h), and Si@SiO_2-PAA-GL electrode (i) after the scratch test.

However, Si@SiO_2-CMC and Si@SiO_2-PAA electrodes show some apparent cracks on their scratched surfaces (Fig. 4g and h). The results are consistent with that of nano-indentation and peeling test. Moreover, the CV curve of the pure PAA-GL binder was evaluated to investigate the electrochemical stability. As shown in Fig. S4, there are no peaks of the oxidation and reduction from CV curve of the pure PAA-GL binder, demonstrating that the PAA-GL binder is inert from 0.01 to 1.0 V versus Li/Li^+. In general, the PAA-GL binder with strong mechanical property can effectively enhance the stability of electrode and improve the electrochemical performance.

The Si@SiO_2-PAA-GL electrode has structural advantages and excellent mechanical properties, which are conductive to Li-ion storage. Electrochemical performances were tested using coin cells. The electrochemical performances of Si@SiO_2 electrode with different binders are depicted in Fig. 5. Fig. 5a presents the CV curve of Si@SiO_2-PAA-GL electrode at 0.02 mV s^{-1}. In the first cathodic process (inset of Fig. 5a), the peak around 1.45 V is assigned to the irreversible reactions between Li ions and SiO_2 (SiO_2+4 Li^++4 e^-→Si+ 2 Li_2O) [46]. Another wide peak around 0.6 V is ascribed to the generation of SEI film owing to the decomposition of electrolyte [47]. The two peaks disappear in the following cycles, revealing that a steady SEI film with Li_2O has produced on the surface of Si@SiO_2 nanoparticles [25]. The reduction peak range from 0.25 to 0.01 V is be relevant to the generation of the Li–Si alloys because of the alloying reaction between Si and Li^+ ($Si + 4.4Li^+ + 4.4e^- = Li_{4.4}Si$) [48]. During the subsequent two scans, the reduction peaks are basically unchanged, indicating that the lithiation process from Si to Li–Si alloy phases is reversible. During the anodic process, the two peaks at 0.4 and 0.57 V are presented during the initial and following two cycles, corresponding to the extraction of Li ions from Li–Si alloy phases [25,49].

The first discharge-charge curves of Si@SiO_2 electrodes with diverse binders are illustrated in Fig. 5b. In the discharge profiles of the Si@SiO_2 electrodes, a flat plateau at the voltage around 0.1 V is found, which can be explained by the Li ions insertion activities. Furthermore, a plateau from 0.40 V to 0.55 V can be seen in the charge curves, corresponding to the deintercalation process of Li ions from Li–Si composites, in line with the result of CV. In addition, in the first cycling process, the Si@SiO_2-PAA-GL electrode delivers high initial discharge and charge capacities of

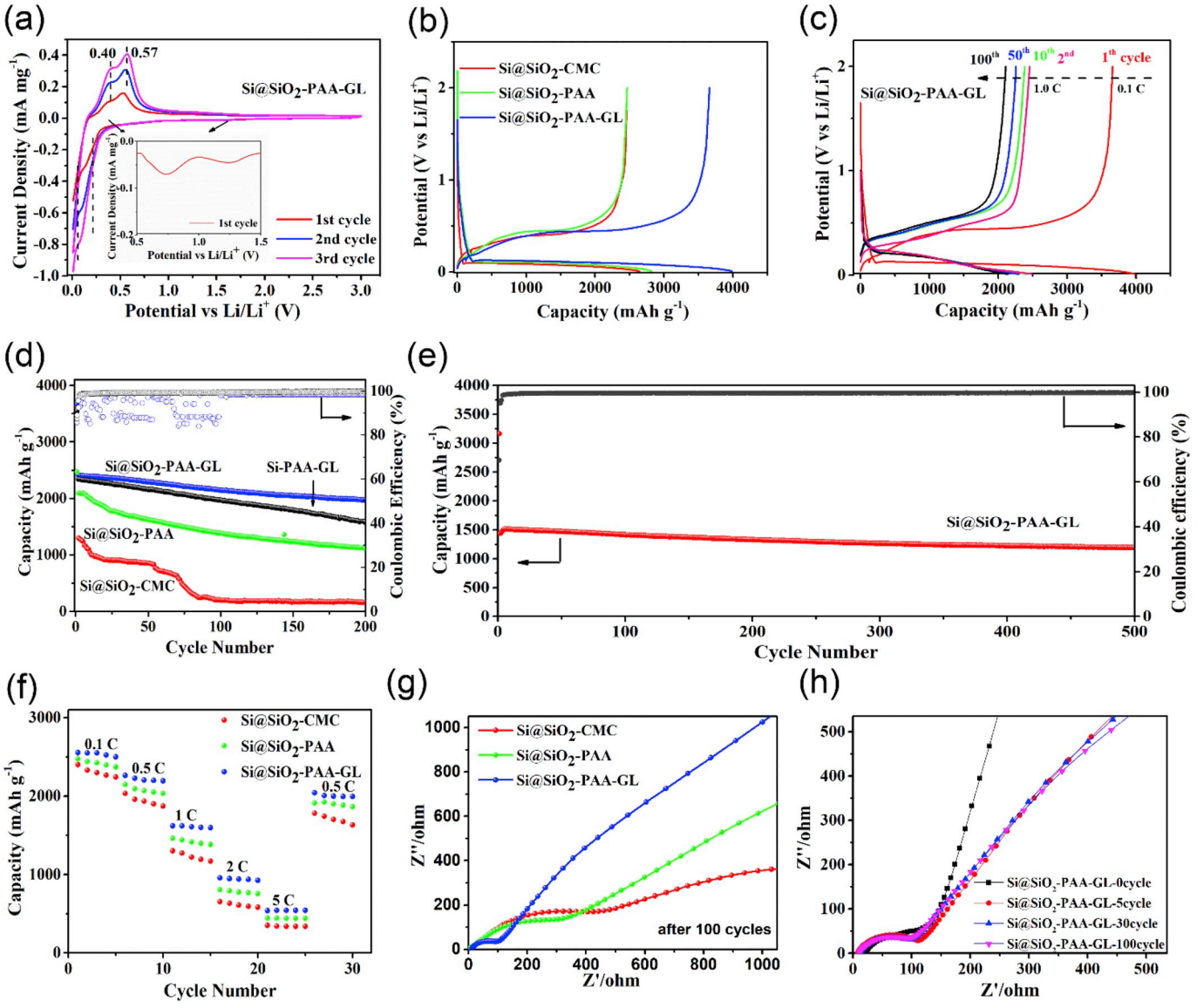

Fig. 5. (a) CV curves of the Si@SiO_2-PAA-GL electrode at the scan rate of 0.2 mV s^{-1}. (b) The initial charging-discharging profiles of Si@SiO_2 electrodes with different binders. (c) Cycling performance at the current density of 1 C. (d) The representative discharge/charge profiles of the Si@SiO_2-PAA-GL electrode. (e) Long cycling lifetime of the Si@SiO_2-PAA-GL electrodes at the current density of 2 C. (f) Rate performance at different rates (from 0.1 to 5 C). (g) EIS plots of Si@SiO_2 electrodes with different binders after 100 cycles. (h) EIS plots of Si@SiO_2-PAA-GL electrodes for different cycles.

3983.2 and 3659.4 mA h g^{-1}, corresponding to an initial Coulombic efficiency (ICE) of 88.87%, larger than that of Si@SiO_2-CMC electrode (2645.71/2457.16 mA h g^{-1}, 85.6%) and Si@SiO_2-PAA electrode (2824.3/2467.18 mA h g^{-1}, 87.35%). Meanwhile, the ICE of Si@SiO_2-PAA-GL electrode fastly augments to 98.4% upon the third cycle (Fig. 5d), higher than 92.77% of Si@SiO_2-CMC and 97.7% of Si@SiO_2-PAA electrode, demonstrating a stable SEI layer formed during cycling. Fig. 5c exhibits the representative charge/discharge curves of the Si@SiO_2-PAA-GL electrode. The first cycle charge/discharge was tested at the current density of 0.1 C. The subsequent cycles (the 2nd, 10th, 50th, and 100th) investigated at the current density of 1.0 C shows no obvious changes, suggesting the high reversibility and good cycling stability of Si@SiO_2-PAA-GL electrode.

The cycling lifetime of Si@SiO_2 electrode with diverse binders are studied by charge/discharge experiments at 1.0 C (Fig. 5d). The Si@SiO_2-PAA-GL electrode displays higher specific capacity during cycling process, compared with Si@SiO_2-CMC and Si@SiO_2-PAA electrodes. After 200 cycles, the Si@SiO_2-PAA-GL electrode still delivers specific capacity of 1975.87 mA h g^{-1}, while the specific capacity of Si@SiO_2-CMC and Si@SiO_2-PAA electrodes are 159.55 and 1117.36 mA h g^{-1}, respectively, confirming the improvement of cyclic performance and capacity for the electrode by the application of the PAA-GL binder. Furthermore, in order to further explore the principle of the modified binder, Si-PAA-GL electrode also was tested. The discharge capacity of Si@SiO_2-PAA-GL and the Si-PAA-GL electrodes still be reserved around 1975.87 and 1541.05 mA h g^{-1} after 200 cycles. The Si@SiO_2-PAA-GL electrode displays the better cyclic stability than Si-PAA-GL electrode due to the improved adhesion between the binder and SiO_2 layers. In addition, the amorphous SiO_2 layer on the surface of Si particles as a snubber region not only can relieves the stress of volume charge but also contribute to the formation of SEI films [44].

Fig. 5e presents the long-term cycling of the Si@SiO_2-PAA-GL electrode at the current density of 2.0 C. The capacity still maintains to be 1203 mA h g^{-1} after 500 cycles. It is worth noting that the capacity decay rate of the Si@SiO_2-PAA-GL electrode is only 0.0337% per cycle, which is more remarkable compared with the previous reports about Si anodes (Table S1). The good cyclability of Si@SiO_2-PAA-GL is ascribed to the improved adhesive strength between Si@SiO_2 and PAA-GL binder, resulting in excellent mechanical property for maintaining integrity of the electrode. In addition, the SiO_2 coating buffers the huge volume change and promotes to form stable SEI.

The rate performance are shown in Fig. 5f, delivering superior kinetics of Si@SiO_2 electrode with -PAA-GL binder. The capacities of the Si@SiO_2-PAA-GL electrode are 2553.3, 2263.8, 1619.0, 955.9, and 538.2 mA h g^{-1} at 0.1, 0.5, 1.0, 2.0, and 5.0 C, respectively; and the capacities of Si@SiO_2 electrode with PAA binder are 2476.6, 2149.3, 1460.1, 804.9, and 443.6 mA h g^{-1}, respectively; while the capacities of the Si@SiO_2-CMC electrode are 2399.8, 2034.7, 1873.0, 653.9, and 349.6 mA h g^{-1}, respectively. Moreover, the capacity retention of Si@SiO_2-PAA-GL electrode is larger than that Si@SiO_2 electrode with CMC and PAA binders, confirming better reversibility for Si@SiO_2-PAA-GL electrode (Fig. S5). The excellent rate performance of the Si@SiO_2-PAA-GL electrode is related to the integrated structure of electrode.

To further acquire dynamic data on Si@SiO_2 based electrode, EIS was carried out. As shown in Fig. 5g and h, the Nyquist plots deliver a depressed semicircle in high frequency region and a quasi-straight line in low frequency region. Obviously, the semicircle diameter of the Si@SiO_2-PAA-GL electrode is lower than that of Si@SiO_2 electrode with CMC and PAA binders after 100 cycles, demonstrating its smaller interfacial resistance. Moreover, the curve slope of the Si@SiO_2-PAA-GL is steeper than that of the Si@SiO_2-CMC and Si@SiO_2-PAA, suggesting that the Li ions transport are faster in the Si@SiO_2-PAA-GL electrode. Besides, in terms of Si@SiO_2-PAA-GL electrode, the interfacial resistance has no obvious changes after 5, 30, and 100 cycles (Fig. 5h), lower than that of Si@SiO_2-CMC and Si@SiO_2-PAA electrodes (Fig. S6). The EIS results can be ascribed to the stable SEI film and structure of electrode with the cross-linked PAA-GL binder.

The structural stability of the electrode is crucial for the cycling performance. To estimate the stability of the electrodes after cycling, the surface morphology, structure, and chemical composition of electrodes with different binders were performed by SEM and XPS. As plotted in Fig. 6a–c, no apparent difference is observed for the Si@SiO_2-PAA-GL electrodes with different binders before cycling. After 100 cycles, as plotted in Fig. 6d and e, huge micron-sized cracks are observed on the surface of CMC and PAA based electrodes because of the huge volume change of Si particles. On the contrary, no evident cracks are found on the Si@SiO_2-PAA-GL electrode (Fig. 6f), suggesting that the electrode with PAA-GL binder efficiently accommodates the volumetric expansion of Si to the greatest extent during cycling. Additionally, the pattern and shape of Si@SiO_2 particles are hardly to identify, suggesting that the thick SEI film is coated on the surface of Si@SiO_2 of CMC and PAA based electrodes (Fig. 6g and h). The thick and unstable SEI films certainly cause negative effect on the electrochemical performances [49]. On the contrary, the boundary and morphology of Si@SiO_2 particles are still clear in the Si@SiO_2-PAA-GL electrode, suggesting that the SEI film is very thin and uniform (Fig. 6i), which is conductive to enhance the cycling stability. In brief, the outstanding structural stability of Si@SiO_2-PAA-GL electrode can be attributed to the robust network of cross-linked binder and high adhesion among the Si particles, Super P, and Cu foil.

XPS was carried out to further analyze composition of the Si@SiO_2-PAA-GL electrode after cycling. The survey spectrum (Fig. S7) of Si@SiO_2-PAA-GL electrode presents the existence of carbon (C 1s, 286 eV), oxygen (O 1s, 532 eV), and fluorine (F 1s, 685 eV) element. From C 1s spectrum (Fig. 7a), the peak at 286.2 eV corresponds to the bonds of C–O, while the peaks at 287.5 eV is assigned to the bond of C═O [14]. The peak at 288.9 eV is the characteristic of alkali carbonate Li_2CO_3 originated from the SEI film, and the peak at 284.3 eV represents the bonds of C–H and C–C coming from the framework of the binder [14, 34, 50]. In the spectrum of the O 1s (Fig. 7b), the two peaks at 531.2 and 532.8 eV are considered to be the components of the SEI layer such as $ROCO_2Li$ and Li_2CO_3 respectively [50]. In addition, from the spectrum of F 1s (Fig. 7c), the peak at 685.1 eV indicate the existence of LiF, which is a component of the SEI layer and acts an important role in protecting further electrolyte reduction, and the peak at 686.5 eV are derived from $LiPF_6$ [50]. The XPS results further confirm that SEI film with inorganic Li_2CO_3, LiF, and organic Li_2O components is formed on the surface of Si@SiO_2, enhancing the cycling stability.

The outstanding electrochemical performance of the Si@SiO_2-PAA-GL electrode may be ascribed to two aspects: On the one hand, the cross-linked PAA-GL binder is robust enough to tolerate the huge volume change of Si particles. The high mechanical performance PAA-GL binder can effectively combine the Si@SiO_2 particles, conductive Super P, and Cu foil with together, thereby maintaining the good conductivity of Si@SiO_2-PAA-GL electrode and improving the endurance for enormous volume expansion of Si particles. On the other hand, the enhanced interactions between the binder and Si@SiO_2 particles can greatly enhance the structural stability and cycling lifetime. Besides, the SiO_2 coating on the surface of Si is also conductive to accommodate the volumetric change.

4. Conclusion

In summary, we report a glycerol modified polyacrylic acid cross-linked binder for high performance silicon based anode. The method to synthesize PAA-GL binder is facile and environmental friendly. Besides, a SiO_2 coating is induced on the surface of Si nanoparticles. The multicomponent Si@SiO_2-PAA-GL electrode is fabricated and proved to be a hopeful anode material for LIBs. Combined with the cross-linked PAA-GL binder and SiO_2 coating, the Si@SiO_2-PAA-GL electrode shows excellent electrochemical performance. The reasons for the good performance can be mainly summarized as follows: (1) The free carboxyl

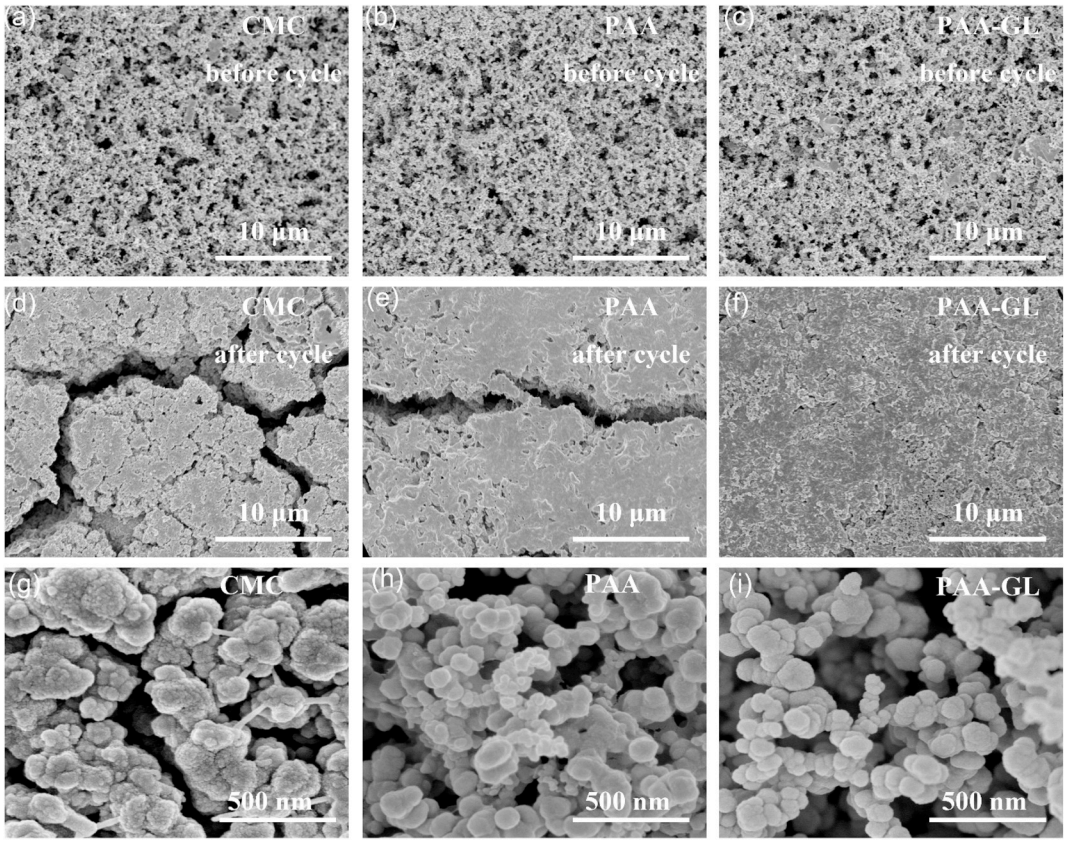

Fig. 6. (a–c) SEM images of the Si@SiO_2-CMC (a), Si@SiO_2-PAA (b), and Si@SiO_2-PAA-GL (c) electrodes before cycle. (d–f) SEM images of the Si@SiO_2-CMC (d), Si@SiO_2-PAA (e), and Si@SiO_2-PAA-GL (f) electrodes after 100 cycles in the scale of micron meter. (g–i) Magnified SEM images of the Si@SiO_2-CMC (g), Si@SiO_2-PAA (h), and Si@SiO_2-PAA-GL (i) electrodes after 100 cycles in the nanometer scale.

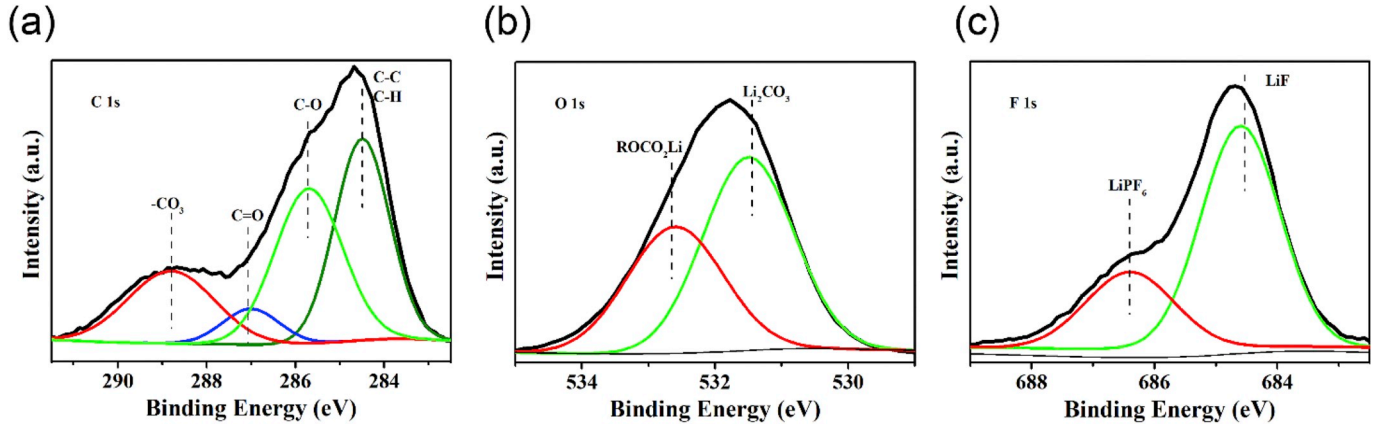

Fig. 7. XPS spectra of C1s (a), O1s (b), and F1s (c) for Si@SiO_2-PAA-GL.

groups of PAA-GL binder and hydroxyl of Si@SiO_2 generate an robust covalent bond. (2) The abundant functional groups from PAA-GL binder offer a strong adhesion for the Si@SiO_2-PAA-GL electrode. (3) The SiO_2 coating can accommodate the huge volume changes of Si nanoparticles. Benefiting from these advantages, the electrode with PAA-GL binder exhibits outstanding structural and cyclic stability. A high capacity of 1192.7 mA h g^{-1} is obtained after 500 cycles at a current density of 2.0 C with a very small capacity decay ratio of 0.0337% % per cycle.

Declaration of competing interest

The authors declare that they have no known competing financial interests or personal relationships that could have appeared to influence the work reported in this paper.

CRediT authorship contribution statement

Sen Sun: Conceptualization, Data curation, Formal analysis, Writing - original draft, Writing - review & editing. **Donglin He:** Conceptualization, Data curation, Formal analysis, Writing - original draft, Writing - review & editing. **Ping Li:** Validation, Formal analysis, Writing - review & editing, Supervision, Project administration, Funding acquisition. **Ying Liu:** Resources, Writing - review & editing, Supervision, Data curation. **Qiwei Tan:** Writing - review & editing. **Zhiwei Liu:** Writing -

review & editing. **Fuqiang An:** Writing - review & editing. **Gaoxiang Gong:** Writing - review & editing. **Xuanhui Qu:** Writing - review & editing, Validation, Supervision, Project administration, Funding acquisition.

Acknowledgements

This study was financially supported by the Major Program Foundation of Shanxi Province (20181102005) and China Postdoctoral Science Foundation (2018M631335). The characterization results were supported by the Beijing Zhongkebaice Technology Service Co.,Ltd. The authors would like to thank Weiwei Chen from Shiyanjia Lab (www.shiyanjia.com) for the TEM analysis.

Appendix A. Supplementary data

Supplementary data to this article can be found online at https://doi.org/10.1016/j.jpowsour.2020.227907.

References

[1] H. Sun, G. Xin, T. Hu, M. Yu, D. Shao, X. Sun, J. Lian, Nat. Commun. 5 (2014) 4526.
[2] C. Wang, H. Wu, Z. Chen, M.T. McDowell, Y. Cui, Z.A. Bao, Nat. Chem. 5 (2013) 1042–1048.
[3] C.K. Chan, H. Peng, G. Liu, K. McIlwrath, X.F. Zhang, R.A. Huggins, Y. Cui, Nat. Nanotechnol. 3 (2008) 31–35.
[4] M. Armand, J.M. Tarascon, Nature 451 (2008) 652–657.
[5] S. Zhu, J.J. Li, X.Y. Deng, C.N. He, E.Z. Liu, F. He, C.S. Shi, N.Q. Zhao, Adv. Funct. Mater. 27 (2017) 1605017.
[6] C.K. Chan, R. Ruffo, S.S. Hong, Y. Cui, J. Power Sources 189 (2009) 1132–1140.
[7] M.T. McDowell, S.W. Lee, W.D. Nix, Y. Cui, Adv. Mater. 25 (2013) 4966–4984.
[8] L. Zhang, R. Rajagopalan, H.P. Guo, X.L. Hu, S.X. Dou, H.K. Liu, Adv. Funct. Mater. 26 (2016) 440–446.
[9] X.X. Zuo, J. Zhu, P. Muller-Buschbaum, Y.J. Cheng, Nano Energy 31 (2017) 113–143.
[10] N. Liu, Z.D. Lu, J. Zhao, M.T. McDowell, H.W. Lee, W.T. Zhao, Y. Cui, Nat. Nanotechnol. 9 (2014) 187–192.
[11] C.K. Chan, R.N. Patel, M.J. O'Connell, B.A. Korgel, Y. Cui, ACS Nano 4 (2010) 1443–1450.
[12] D. Shao, D. Tang, Y. Mai, L. Zhang, J. Mater. Chem. 1 (2013) 15068–15075.
[13] H.C. Shim, I. Kim, C.S. Woo, H.J. Lee, S. Hyun, Nanoscale 9 (2017) 4713–4720.
[14] C.C. Nguyen, T. Yoon, D.M. Seo, P. Guduru, B.L. Lucht, ACS Appl. Mater. Interfaces 8 (2016) 12211–12220.
[15] R. Yi, F. Dai, M.L. Gordin, S.R. Chen, D.H. Wang, Adv. Energy Mater. 3 (2013) 295–300.
[16] D. Lin, Y. Liu, Z. Liang, H.-W. Lee, J. Sun, H. Wang, K. Yan, J. Xie, Y. Cui, Nat. Nanotechnol. 11 (2016) 626–632.
[17] H. Zhao, Y. Wei, C. Wang, R.M. Qiao, W.L. Yang, P.B. Messersmith, G. Liu, ACS Appl. Mater. Interfaces 10 (2018) 5440–5446.
[18] Y. Chen, L. Bao, N. Du, T. Yang, Q. Mao, X. Lu, Y. Lin, Z. Ji, Nanotechnology 30 (2019), 035602.
[19] Y.L. Chen, Y. Hu, Z. Shen, R.Z. Chen, X. He, X.W. Zhang, Y.Q. Li, K.S. Wu, J. Power Sources 342 (2017) 467–475.
[20] L. Sun, T. Su, L. Xu, M. Liu, H.-B. Du, Chem. Commun. 52 (2016) 4341–4344.
[21] J. Bae, D.S. Kim, E. Park, M.-S. Park, H. Kim, Bull. Kor. Chem. Soc. 37 (2016) 1039–1043.
[22] J.H. Yom, J.K. Lee, W.Y. Yoon, J. Appl. Electrochem. 45 (2015) 397–403.
[23] M.-J. Jung, K.-Y. Sheem, Y.-S. Lee, J. Nanosci. Nanotechnol. 14 (2014) 2852–2858.
[24] Y. Hwa, C.M. Park, H.J. Sohn, J. Power Sources 222 (2013) 129–134.
[25] C. Luo, L.L. Du, W. Wu, H.L. Xu, G.Z. Zhang, S. Li, C.Y. Wang, Z.G. Lu, Y.H. Deng, ACS Sustain. Chem. Eng. 6 (2018) 12621–12629.
[26] Y. Shi, L.J. Pan, B.R. Liu, Y.Q. Wang, Y. Cui, Z.A. Bao, G.H. Yu, J. Mater. Chem. 2 (2014) 6086–6091.
[27] D.H. Yao, Y. Yang, Y.H. Deng, C.Y. Wang, J. Power Sources 379 (2018) 26–32.
[28] X.Y. Zhu, F. Zhang, L. Zhang, L.Y. Zhang, Y.Z. Song, T. Jiang, S. Sayed, C. Lu, X. G. Wang, J.Y. Sun, Z.F. Liu, Adv. Funct. Mater. 28 (2018) 1705015.
[29] Z.G. Zhang, Y. Jiang, Z. Peng, S.S. Yang, H. Lin, M. Liu, D.Y. Wang, ACS Appl. Mater. Interfaces 9 (2017) 32775–32781.
[30] J. Li, G. Zhang, Y. Yang, D. Yao, Z. Lei, S. Li, Y. Deng, C. Wang, J. Power Sources 406 (2018) 102–109.
[31] M. Ling, Y.N. Xu, H. Zhao, X.X. Gu, J.X. Qiu, S. Li, M.Y. Wu, X.Y. Song, C. Yan, G. Liu, S.Q. Zhang, Nano Energy 12 (2015) 178–185.
[32] P.F. Cao, M. Naguib, Z.J. Du, E. Stacy, B.R. Li, T. Hong, K.Y. Xing, D.N. Voylov, J. L. Li, D.L. Wood, A.P. Sokolov, J. Nanda, T. Saito, ACS Appl. Mater. Interfaces 10 (2018) 3470–3478.
[33] Y. Liu, Z. Tai, T. Zhou, V. Sencadas, J. Zhang, L. Zhang, K. Konstantinov, Z. Guo, H. K. Liu, Adv. Mater. 29 (2017) 1703028.
[34] L. Yue, L.Z. Zhang, H.X. Zhong, J. Power Sources 247 (2014) 327–331.
[35] S.-J. Park, H. Zhao, G. Ai, C. Wang, X. Song, N. Yuca, V.S. Battaglia, W. Yang, G. Liu, J. Am. Chem. Soc. 137 (2015) 2565–2571.
[36] B. Hu, I.A. Shkrob, S. Zhang, L.H. Zhang, J.J. Zhang, Y. Li, C. Liao, Z.C. Zhang, W. Q. Lu, L. Zhang, J. Power Sources 378 (2018) 671–676.
[37] B. Koo, H. Kim, Y. Cho, K.T. Lee, N.S. Choi, J. Cho, Angew. Chem. Int. Ed. 51 (2012) 8762–8767.
[38] J.X. Song, M.J. Zhou, R. Yi, T. Xu, M.L. Gordin, D.H. Tang, Z.X. Yu, M. Regula, D. H. Wang, Adv. Funct. Mater. 24 (2014) 5904–5910.
[39] H. Wu, G. Yu, L. Pan, N. Liu, M.T. McDowell, Z. Bao, Y. Cui, Nat. Commun. 4 (2013) 1943.
[40] H. Zhao, Y. Wei, R.M. Qiao, C.H. Zhu, Z.Y. Zheng, M. Ling, Z. Jia, Y. Bai, Y.B. Fu, J. L. Lei, X.Y. Song, V.S. Battaglia, W.L. Yang, P.B. Messersmith, G. Liu, Nano Lett. 15 (2015) 7927–7932.
[41] J. Liu, Q. Zhang, T. Zhang, J.T. Li, L. Huang, S.G. Sun, Adv. Funct. Mater. 25 (2015) 3599–3605.
[42] J. Ryu, D. Hong, S. Choi, S. Park, ACS Nano 10 (2016) 2843–2851.
[43] J.S. Kim, W. Pfleging, R. Kohler, H.J. Seifert, T.Y. Kim, D. Byun, H.-G. Jung, W. Choi, J.K. Lee, J. Power Sources 279 (2015) 13–20.
[44] S.T. Guo, H. Li, Y.Q. Li, Y. Han, K.B. Chen, G.Z. Xu, Y.J. Zhu, X.L. Hu, Adv. Energy Mater. 8 (2018) 1800434.
[45] M. Wu, X. Xiao, N. Vukmirovic, S. Xun, P.K. Das, X. Song, P. Olalde-Velasco, D. Wang, A.Z. Weber, L.W. Wang, V.S. Battaglia, W. Yang, G. Liu, J. Am. Chem. Soc. 135 (2013) 12048–12056.
[46] Y. Chen, L.F. Liu, J. Xiong, T.Z. Yang, Y. Qin, C.L. Yan, Adv. Funct. Mater. 25 (2015) 6701–6709.
[47] Y. Zhao, L. Yang, Y. Zuo, Z. Song, F. Liu, K. Li, F. Pan, ACS Appl. Mater. Interfaces 10 (2018) 27795–27800.
[48] J.Y. Ji, H.X. Ji, L.L. Zhang, X. Zhao, X. Bai, X.B. Fan, F.B. Zhang, R.S. Ruoff, Adv. Mater. 25 (2013) 4673–4677.
[49] D. Shao, H.X. Zhong, L.Z. Zhang, Chemelectrochem 1 (2014) 1679–1687.
[50] P. Verma, P. Maire, P. Novak, Electrochim. Acta 55 (2010) 6332–6341.